Materials Advances

ROYAL SOCIETY OF CHEMISTRY

PAPER

Check for updates

Improved thermoelectric performance of Co-doped β-FeSi₂ by Ni substitution†

Sopheap Sam, [ID] [a] Hiroshi Nakatsugawa [ID] *[a] and Yoichi Okamoto[b]

Employing thermoelectric (TE) materials, which can directly convert heat into electricity, are a promising strategy for recovering industrial waste heat. Currently, TE materials with an acceptable conversion performance are expensive and toxic. Therefore, this work aims to enhance the TE performance of inexpensive and eco-friendly Co-doped iron silicide compounds by Ni addition. The investigation of the structural, electrical, and TE characteristics of Ni-alloyed β-Fe$_{0.97-x}$Ni$_x$Co$_{0.03}$Si$_2$ (x = 0, 0.005, 0.01, 0.02, and 0.03) fabricated by the arc-melting process is reported in this study. The results show that the metallic ε-phase increased with x, resulting in a decrease in the solubility of the Ni and Co alloy material. However, the mobility (μ_H) significantly improved from 3.5(6) up to 25(5) cm^2 V^{-1} s^{-1} with Ni substitution, which is 7 times higher than the x = 0 sample. At high temperatures, the electrical resistivity of the Ni-substituted samples was remarkably lower than that of the x = 0 sample owing to the enhancement of μ_H. The presence of the ε-phase induced a negative impact on the Seebeck coefficient, and the thermal conductivity slightly decreased with x because of the increase in porosity. As a result, the optimum condition to improve the power factor and dimensionless figure of merit was achieved in the x = 0.01 sample with the maximum PF$_{max}$ of 2400 μW m^{-1} K^{-2} and ZT_{max} of 0.31, indicating a three-fold enhancement compared with the x = 0 sample.

1. Introduction

Thermoelectric (TE) generator, a solid-state device, is one of the promising solutions for harvesting the excess heat dissipated by the exhaust systems of various industrial plants[1,2] and automobiles[3–5] and directly converting it to electricity without employing any moving parts and causing gas pollution. The efficiency of the TE device is mainly proportional to the performance of the assembled TE materials, which is evaluated by the dimensionless figure of merit (ZT) according to eqn (1):

$$ZT = S^2\rho^{-1}\kappa^{-1}T \qquad (1)$$

where S, ρ, κ, and T represent the Seebeck coefficient, electrical resistivity, total thermal conductivity, and temperature, respectively.[6] The term $S^2\rho^{-1}$ is usually assigned as the power factor (PF = $S^2\rho^{-1}$), and the total thermal conductivity is the sum of the lattice and carrier thermal conductivity components ($\kappa = \kappa_1 + \kappa_e$). Bi$_2Te_3$ and PbTe are traditional TE materials that are known for toxicity and high price. To solve this issue, researchers have been striving to improve the performance of

low-cost, less-toxic, and eco-friendly compounds, such as oxides,[7–10] sulfides,[11,12] Heusler intermetallic alloys,[13,14] and iron silicide.[15–18] Among these materials, iron silicide is an attractive material to use at high temperatures because of its stable thermal properties and ability to withstand oxidation.[19] Notably, iron silicide has three different phases, namely α-phase (α-Fe$_2$Si$_5$ crystallizes with a tetragonal structure and the space group of $P4/mmm$),[15] ε-phase (ε-FeSi crystallizes with a cubic structure and the space group of $P2_13$),[16] and β-phase (β-FeSi$_2$ crystallizes with an orthorhombic structure and the space group of $Cmce$).[17] The phase transition of this material is dependent on the condition of heat treatment and the amount and kind of external impurity added, while pure β-FeSi$_2$ can be grown at temperatures below 1259 K, and α and ε-phases are formed above 1259 K.[20] The ε and α-phases are metallic phases[21] and are not suitable as TE materials because of the low Seebeck coefficient (S). Therefore, only the semiconducting β-phase with a narrow energy gap (E_g = 0.7 eV) is favorable for TE research.[22] It has been noted that the TE performance of pure β-FeSi$_2$ is still low owing to its high κ and low PF. Therefore, previous studies attempted to minimize the κ of β-FeSi$_2$ by introducing stacking fault,[23] doping with heavy elements,[24,25] rapid solidification and hot pressing to reduce grain size,[26] and other nano-structuring techniques.[27] On the other hand, the PF value of β-FeSi$_2$ is low due to the high ρ and low $|S|$ in the high-temperature regions, where the bipolar

[a] Yokohama National University, Yokohama 240-8501, Japan.
  E-mail: nakatsugawa-hiroshi-dx@ynu.ac.jp
[b] National Defense Academy, Yokosuka 239-8686, Japan

† Electronic supplementary information (ESI) available. See DOI: https://doi.org/10.1039/d3ma00153a

effect occurs because of a low carrier density (n_H) of about 10^6 cm^{-3} and a small band gap of about 0.7 eV. This bipolar effect can be reduced by increasing n_H with the addition of appropriate external impurities and consequently, the $|S|$ can be enhanced.[28–30] Based on Drude's theory of semiconductors, the increase in n_H can simultaneously reduce ρ. In other words, by alloying β-FeSi$_2$ with appropriate impurities that have different valence electrons to occupy the Fe or Si site, an improvement in the PF and ZT value of β-FeSi$_2$ can be effectively obtained. Hence, researchers have been trying to improve the TE properties of binary β-FeSi$_2$ by alloying it with various elements.

Zhao *et al.* reported that Mn-doped β-Fe$_{1-x}$Mn$_x$Si$_2$ prepared by the hot-pressing method exhibited a maximum ZT of 0.17 at 837 K. This maximum ZT value was mainly caused by the improvement in PF.[31] In addition, the maximum ZT of 0.6 at 1173 K was obtained by doping 16% Ir in β-FeSi$_2$. The improved ZT of Ir-doped β-FeSi$_2$ is influenced by the significant reduction in electrical resistivity due to the high carrier density of 1.1×10^{22} cm^{-3} and reduction in thermal conductivity.[32] More importantly, the electrical conductivity of β-FeSi$_2$ was effectively improved by alloying it with Co or Ni, which caused an increase in n_H, as reported by Tani *et al.*[33] Since the n_H could be significantly increased by Co substitution, they further attempted to investigate the thermoelectric properties of β-Fe$_{1-x}$Co$_x$Si$_2$ fabricated by the spark plasma sintering (SPS) method. The maximum PF of around 1.1×10^{-5} W cm^{-1} K^{-2} was obtained in the $x = 0.05$ sample, and the maximum ZT was 0.25 at 940 K. Notably, κ was also slightly reduced probably due to electron–phonon interactions.[34] In addition, they further aimed to enhance the TE properties by substituting Pt in the Fe site of β-Fe$_{1-x}$Pt$_x$Si$_2$. The solubility limit of Pt in the base material was about 2%, and the highest ZT of 0.14 at 847 K was obtained in the $x = 0.03$ sample mainly contributed by the enhancement in PF due to the reduction in ρ.[35] The investigation of P addition in β-FeSi$_2$ was reported by Ito *et al.* The ball milling and hot-pressed techniques were used to fabricate the samples. All P-doped samples showed n-type semiconductor characteristics, and the maximum ZT of around 0.033 was achieved in the 2% P-doped sample due to the improved PF.[36] Redzuan *et al.* reported that the Fe$_{28.49}$Co$_{0.59}$Si$_{70.5}$ sample prepared by the pressure-sintering method had the highest ZT of 0.085 at 1073 K.[37] In addition, the influence of various impurities, such as Mn, Al, P, and Co, on β-FeSi$_2$ prepared by mechanical milling followed by the pulse plasma sintering (PPS) technique was investigated by Dabrowski *et al.* It presented the highest ZT of around 0.15 with 3% Co addition probably because of the increase in carrier density, leading to a significant decrease in ρ and an increase in PF.[38]

In line with the previous studies, Co can be considered an appropriate impurity for the enhancement of TE properties of β-FeSi$_2$ as it results in enhanced PF. In addition, we recently investigated the optimum Co doping amount for improving the TE properties of β-Fe$_{1-x}$Co$_x$Si$_2$ fabricated by the arc-melting method. The maximum PF of 900 μW m^{-1} K^{-1} and ZT of 0.099 were obtained for β-Fe$_{0.97}$Co$_{0.03}$Si$_2$. However, the tendency of ρ of this Co-doped sample was uniform over the temperature

range of 300–800 K. This is probably due to the low mobility (μ_H) of around 3.5 cm^2 V^{-1} s^{-1}.[39] Interestingly, it has been reported that the tendency of ρ of Ni-doped β-Fe$_{1-x}$Ni$_x$Si$_2$ decreases with increasing temperature probably due to the higher μ_H in the range of 10–35 cm^2 V^{-1} s^{-1}.[40] Since we have previously found that the maximum ZT was obtained in the β-Fe$_{0.97}$Co$_{0.03}$Si$_2$ matrix prepared by arc-melting followed by a heat treatment process,[39] we attempt to improve the performance of β-Fe$_{0.97}$Co$_{0.03}$Si$_2$ prepared by the same fabrication process by alloying it with Ni in this work. When an appropriate amount of Ni is added to β-Fe$_{0.97}$Co$_{0.03}$Si$_2$, the μ_H is expected to increase. As a result, the ρ can be further decreased and additional enhancement of the PF and ZT values can be obtained.

This work aims to improve the carrier mobility of the iron silicide-based material by co-doping of Co and Ni, which can enhance its thermoelectric performance. We also present the effects of Ni addition on the structural, electrical, and TE characteristics (electrical resistivity, Seebeck coefficient, power factor, thermal conductivity, and ZT values) of non-doped β-FeSi$_2$ and β-Fe$_{0.97-x}$Ni$_x$Co$_{0.03}$Si$_2$ ($x = 0$, 0.005, 0.01, 0.02, and 0.03) fabricated by the arc-melting process. From 80–800 K, the TE properties of the fabricated materials are reported in detail. The Ni concentration has been optimized for improving the TE properties.

2. Experimental methods

2.1 Fabrication method

The compounds non-doped FeSi$_2$ and Fe$_{0.97-x}$Ni$_x$Co$_{0.03}$Si$_2$ ($x = 0.005$, 0.01, 0.02, and 0.03) were prepared using raw elements, including iron (Fe, 99.9% up, grain), silicon (Si, 99.999%, grain), nickel (Ni, 99.9%, grain), and cobalt (Co, 99% up, powder), purchased from High Purity Chemicals in Japan. After weighing each of them according to the composition ratio, the arc-melting process was used to melt the raw materials in an Ar atmosphere under a pressure of 10^{-3} Pa. Before melting the key materials, 10 g of titanium was melted to react with the residual O$_2$ in the melting chamber. To ensure homogeneous material distribution, the ingots were flipped, and the melting process was repeated three times. The ingots obtained from the arc-melting process were in the metallic phase (ε-FeSi + α-Fe$_2$Si$_5$). To transform these metallic phases into β-phase, heat treatment was necessarily applied. The numerical control wire-cutting machine (EC-3025, Makino) was used to slice the ingots into samples of appropriate size (7 mm × 7 mm × 1.5 mm) to characterize the thermoelectric properties. All surfaces of the sliced samples were then polished to remove contamination during the early cutting process. After that, each sample was vacuum-sealed inside a quartz ampule, and the carbon sheet was also set together with it to react with the residual oxygen. After vacuum-sealing, it was heat-treated in an electrical furnace at 1423 K for 3 hours to further homogenize the distribution of materials, followed by treatment at 1113 K for 20 hours to transform the metallic ε + α

phases into the semiconducting β-phase. This heat treatment condition was optimized according to a previous report.[41]

2.2 Characterization method

The X-ray diffraction (XRD) measurements were performed using a high-resolution X-ray diffractometer with Cu Kα radiation (High-resolution SmartLab, Rigaku). The crystal parameters were computed by utilizing the Rietveld refinement method in the RIETAN-FP program. In the computation process, the occupation rate of Fe and Ni were set to $0.97 - x$ and x, respectively. The surface microstructure was visualized by using a 3D Real Surface View Microscope (VE-8800, KEYENCE). The elemental analysis was carried out by using a scanning electron microscope (SEM, SU8010, Hitachi High-Technologies) equipped with an energy-dispersive X-ray spectroscopy (EDS XFlash5060FQ, Bruker) detector. The gravity measurement tool (SMK-401, SHIMADZU) was used to measure relative density based on the Archimedes method. The mobility (μ_H) and carrier density (n_H) at 300 K were measured by using the ResiTest8300 apparatus (TOYO Co.). Then, ResiTest8300 and a homebuilt apparatus were used to measure the electrical resistivity (ρ) and Seebeck coefficient (S) from 80–800 K. The power efficiency measurement apparatus (PEM-2, ULVAC) was used to characterize the thermal conductivity (κ).

3. Results and discussion

3.1 Crystal structure

The X-ray diffraction (XRD) patterns of non-doped $FeSi_2$ measured at diffraction angles between $20° \leq 2\theta \leq 90°$ are shown in Fig. 1. Before the heat treatment (after the arc-melting process), non-doped $FeSi_2$ crystallized in the metallic α and ε phases (α-Fe_2Si_5 + ε-FeSi) due to the high melting temperature

produced by the arc power. Fig. 2 shows the Rietveld analysis of all samples after heat treatment. The calculated, experimental, and differential data are denoted by the green, red, and blue lines, respectively. All samples crystallized in the semiconducting β-phase (β-$FeSi_2$ and β-$Fe_{0.97-x}Ni_xCo_{0.03}Si_2$) with a trace of the ε-phase at the diffraction angle of $2\theta \approx 45.2°$. This result suggests that the heat treatment process is necessary for phase transformation in the Fe–Si system. In addition, the ε-phase peak intensity of the $x = 0.01, 0.02, 0.03$ samples were higher than those of the $x = 0$ and 0.005 and pure β-$FeSi_2$ samples, indicating that Ni substitution increases the formation of the ε-phase.

The three-dimensional crystal structure of the $x = 0.01$ sample is shown in Fig. 3. Geometrically, the bounds of the four Si1 and four Si2 atoms were attached in eight coordinates to every site of Fe1 and Fe2, and the Si–Fe distances ranged between 2.303(7)–2.419(6) Å and 2.333(3)–2.398(6) Å, respectively. In addition, the crystal structure parameters of all samples, as calculated by Rietveld analysis, are summarized in Table S1 (ESI†). The reliability factor R_{wp} (weighted diffraction patterns) ranged from 2.907 to 3.474, suggesting a good fit between the calculated and observed intensities. In addition, the variation in the interacting atomic Si–Fe distance and Fe–Si–Fe angles can be found in Fig. S1 (ESI†). In Fig. S1a (ESI†), with increasing x, the Si2–Fe1 and Si2–Fe2 distances are uniform, but the Si1–Fe1 distance slightly declines, and the Si1–Fe2 distance moderately rises. As shown in Fig. S1b (ESI†), with increasing x, the interaction atomic angle of Fe1–Si2–Fe1 and Fe2–Si2–Fe2 were uniform, but the Fe1–Si1–Fe1 slightly rose, and the Fe2–Si1–Fe2 moderately declined. This indicates that Fe1 and Fe2 are equally substituted by Ni.

3.2 Microstructures analysis

Fig. 4 shows the surface morphology of all samples, demonstrating the variation in microstructures. As shown in Fig. 4(a), the ε-phase (bright grain) and α-phase (dark grain) were formed before the heat treatment, confirming the XRD patterns in Fig. 1. The residual dust produced by the polishing process appeared as white dots. Fig. 4(b) and (c) show that after the heat treatment, the bright grains disappeared, indicating that the non-doped $FeSi_2$ and $x = 0$ samples grew homogeneously in the β-phase. However, Fig. 4(d)–(g) show that the addition of Ni caused the appearance of the ε-phase. In addition, the ε-phase grain tended to enlarge when x was increased from 0.005 to 0.03. These SEM images are consistent with that of Rietveld refinement results presented in Fig. 2, in which the peak intensity of the ε-phase increases with x. This tendency is similar to that observed in a previous report when Ni alone is added to the β-$FeSi_2$ system.[40] Moreover, the pore size became larger after the heat treatment process. An increase in pore size is usually observed when phase changes occur during the heat treatment process because the volume of β-$FeSi_2$ differs from those of α-Fe_2Si_5 and ε-FeSi (3β-$FeSi_2 \leftarrow \alpha$-Fe_2Si_5 + ε-FeSi). In addition, as shown in Fig. 4(g), the pores in the $x = 0.03$ sample were more than those in the other samples, indicating that the number of pores increases with Ni content. However, the relative
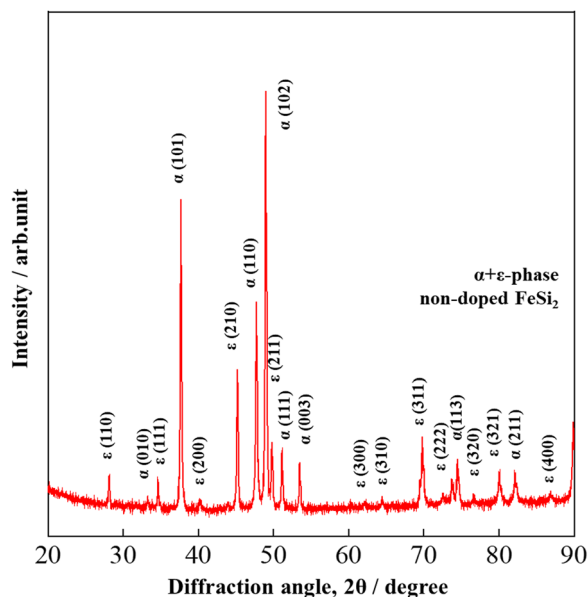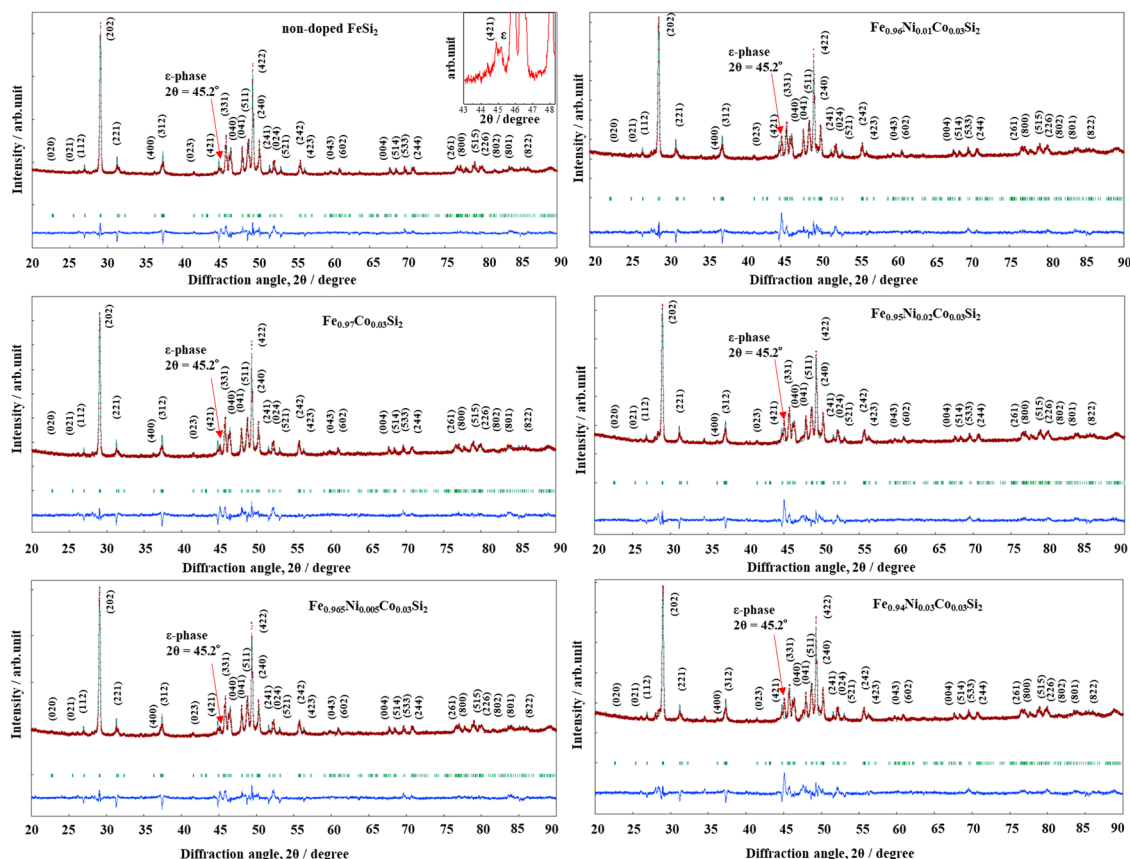

Fig. 1 The XRD patterns of non-doped $FeSi_2$ before heat treatment at room temperature. The indexed peaks are those of ε + α-phases, indicating that metallic phases are formed after the arc-melting process.

Fig. 2 Rietveld analysis of non-doped β-FeSi$_2$ and β-Fe$_{0.97-x}$Ni$_x$Co$_{0.03}$Si$_2$ ($0 \leq x \leq 0.03$) after heat treatment; the indexed peaks are those of the β-phase, and the peak of ϵ-phase is magnified in the inset. The red lines represent experimental data, the green lines indicate calculated data, and the blue lines denote the difference between the datasets. The arrows indicate that the peak of ϵ-phase at $2\theta = 45.2°$ increases with increasing x.
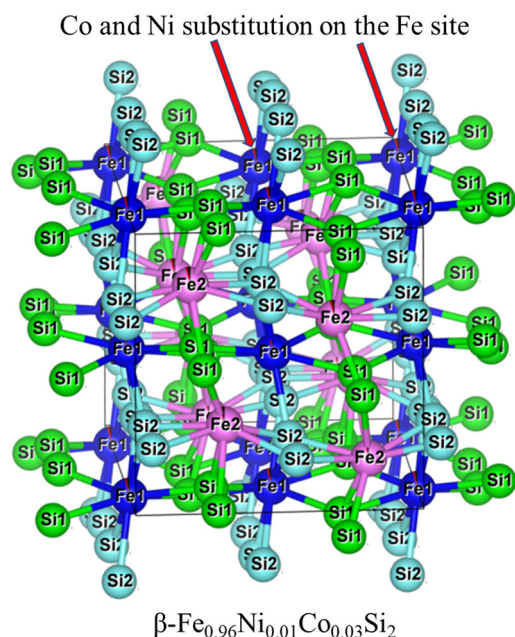

Fig. 3 The three-dimensional crystal structure of β-Fe$_{0.97-x}$Ni$_x$Co$_{0.03}$Si$_2$ ($x = 0.01$).

density of all samples was in the range of 97.2(1)–98.0(1)%, as shown in Table 1. These values of relative density are almost the same as those of the materials fabricated by the hot-pressing technique.[42] However, the densities of materials fabricated by the spark plasma[43,44] and pulse plasma sintering techniques[38,45] are relatively lower than those of our materials. Therefore, it can be considered that samples with high density can be fabricated by the direct arc-melting method with a heat treatment process, which contributes positively to the enhancement of electrical conductivity and consequently improves the TE performance.

3.3 Elemental analysis

The elemental compositions of β-Fe$_{0.97-x}$Ni$_x$Co$_{0.03}$Si$_2$ ($x = 0.005$, 0.01, 0.02, and 0.03) analyzed by SEM-EDS measurements are summarized in Table 2. The result shows that the Fe : Si ratio in the ϵ area was around 1 : 1, representing ϵ-FeSi, and that in the β area was around 1 : 2, representing the β-FeSi$_2$. In addition, the accumulation of Ni in the ϵ area significantly increased with x, indicating that Ni is preferentially distributed in the ϵ-phase. The EDS mapping image in Fig. 5 also shows that Ni accumulated more in the ϵ-phase than in the β-phase, as indicated by the green color. As a result, even at the nominal composition of $x = 0.03$, the actual x in the β grain is only 0.01(1). This tendency
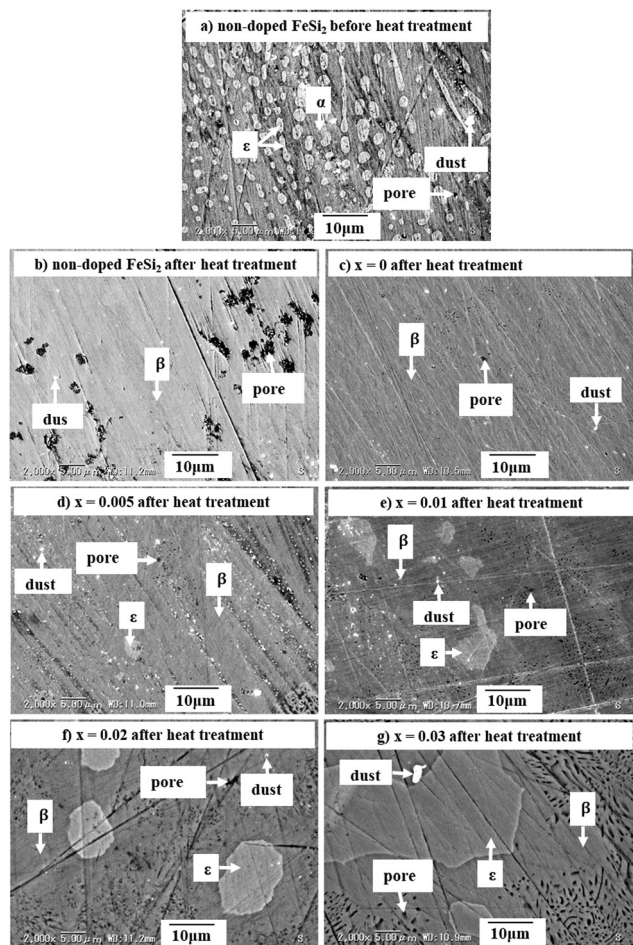
Fig. 4 The SEM micrographs of (a) non-doped β-FeSi$_2$ before heat treatment, (b) non-doped β-FeSi$_2$ after heat treatment, and (c)–(g) β-Fe$_{0.97-x}$Ni$_x$Co$_{0.03}$Si$_2$ after heat treatment.

suggests that 1% could be the maximum solubility of Ni in the β-phase. In addition, Fig. S2 (ESI†) shows that not only Ni but Co also accumulated in the ε-phase, as evidenced by the cyan color. Based on this color mapping, the Co richness in the ε-phase of x = 0.005 (Fig. S2a, ESI†) seemed to be less than that of x = 0.03 (Fig. S2b, ESI†), meaning that the distribution of Co in the host β-FeSi$_2$ becomes less homogenous when more Ni is added or more ε-phases are formed. In other words, when more ε-phases are formed, more Co accumulates in them. Therefore, the amount of Co distributed in β-FeSi$_2$ decreases with increasing Ni.

3.4 Electrical properties

Fig. 6 shows the tendency of carrier density (n_H) and mobility (μ_H) of non-doped β-FeSi$_2$ and β-Fe$_{0.97-x}$Ni$_x$Co$_{0.03}$Si$_2$. As shown in Fig. 6(a), the n_H of the x = 0 sample was about 10^{20} cm^{-3}, which is higher than that of non-doped β-FeSi$_2$, indicating that Co acts as a donor. Importantly, the n_H of the $0.005 \leq x \leq 0.03$ samples were about one order smaller in magnitude than that of the x = 0 sample. It can be considered that Ni triggers the formation of small ε-phases and simultaneously decreases the solubility of Co in the base material, as confirmed by the area of Co richness observed in the EDS mapping analysis. In other words, the improvement in the n_H of the iron silicide compounds is mainly dependent on the solid solution limits of the dopants. However, Fig. 6(b) shows that the μ_H of the $0.005 \leq x \leq 0.03$ samples were 7 times higher than that of the x = 0 sample. This increase in μ_H is probably because of the lighter effective mass (m^*) of Ni than that of Co.[39,40] As seen in Table 1, from x = 0.005 to x = 0.03, the μ_H ranged from 25(5) to 24(3) cm^2 V^{-1} s^{-1}, respectively. These μ_H values are about 80 times higher than that of ruthenium (Ru)-alloyed Co-doped β-FeSi$_2$ prepared by spark plasma sintering,[25] 50 times higher than that of Co- or Ni-doped β-FeSi$_2$ prepared by pressure sintering,[33] and 4 times higher than that of the Co-doped β-FeSi$_2$ single crystal fabricated by the chemical vapor transport method.[46] Therefore, when Ni is introduced to the Co-doped sample, the carrier mobility increases because of its lighter effective mass. The enhanced μ_H values obtained by co-doping of Co and Ni in β-FeSi$_2$ in this work have a positive impact on the reduction in electrical resistivity and improvement of TE properties, as discussed in the next section.

3.5 Thermoelectric properties

Fig. 7 shows the electrical resistivity (ρ) measured over temperatures in the 80–800 K range. Below 300 K, the ρ of the β-Fe$_{0.97-x}$Ni$_x$Co$_{0.03}$Si$_2$ samples were 3 orders smaller in magnitude than that of pristine β-FeSi$_2$ due to the increase in n_H, as shown in Table 1. Drude's formula explains the correlation between ρ and n_H, as shown in eqn (2).

$$\rho = \frac{1}{|e|\mu_H n_H} \quad (2)$$

where e is the elementary charge, μ_H is the mobility, and n_H is the carrier density.[47] An inverse proportionality between ρ and n_H is implied in eqn (2). Hence, the electrical resistivity of pristine β-FeSi$_2$ is much higher than that of other samples.

Table 1 Lorenz number (L_0), carrier density (n_H), mobility (μ_H), relative density, electrical resistivity (ρ), Seebeck coefficient (S), and thermal conductivity (κ) of non-doped β-FeSi$_2$ and β-Fe$_{0.97-x}$Ni$_x$Co$_{0.03}$Si$_2$ at room temperature

Sample name	x	L_0 [V^2 K^{-2}]	n_H [cm^{-3}]	μ_H [cm^2 V^{-1} s^{-1}]	ρ [Ω cm]	S [μ V K^{-1}]	κ [W m^{-1} K^{-1}]	Relative density [%]
Non-doped FeSi$_2$		1.792×10^{-8}	$2.3(5) \times 10^{16}$	37(4)	7.10	−127	7.16	98.0(1)
Fe$_{0.97-x}$Ni$_x$Co$_{0.03}$Si$_2$	0	1.644×10^{-8}	$1.2(4) \times 10^{20}$	3.5(6)	0.015	−213	6.33	97.9(1)
	0.005	1.651×10^{-8}	$1.3(3) \times 10^{19}$	25(5)	0.021	−200	5.67	97.8(1)
	0.01	1.753×10^{-8}	$1.4(3) \times 10^{19}$	25(5)	0.019	−139	5.11	97.6(1)
	0.02	1.837×10^{-8}	$2.0(3) \times 10^{19}$	25(5)	0.013	−116	4.75	97.4 (1)
	0.03	1.862×10^{-8}	$2.2(3) \times 10^{19}$	24(3)	0.012	−111	5.09	97.2(1)

Table 2 The elemental composition of β-$Fe_{0.97-x}Ni_xCo_{0.03}Si_2$ ($0.005 \leq x \leq 0.03$)

x	Area	Element	Atomic%	Composition ratio	Chemical formula
0.005	β	Fe	37.0(3)	1.11(1)	β-$Fe_{1.11(1)}Ni_{0.001(1)}Co_{0.037(1)}Si_{1.85(1)}$
		Ni	0.04(4)	0.001(1)	
		Co	1.24(4)	0.037(1)	
		Si	61.7(2)	1.85(1)	
	ε	Fe	55.7(5)	1.11(1)	ε-$Fe_{1.11(1)}Ni_{0.016(1)}Co_{0.049(3)}Si_{0.82(1)}$
		Ni	0.8(3)	0.016(6)	
		Co	2.4(1)	0.049(3)	
		Si	41.1(6)	0.82(1)	
0.01	β	Fe	39.5(3)	1.18(1)	β-$Fe_{1.18(1)}Ni_{0.005(1)}Co_{0.037(2)}Si_{1.77(1)}$
		Ni	0.18(4)	0.005(1)	
		Co	1.23(7)	0.037(2)	
		Si	59.1(2)	1.77(1)	
	ε	Fe	54.5(7)	1.09(1)	ε-$Fe_{1.09(1)}Ni_{0.015(1)}Co_{0.038(1)}Si_{0.86(1)}$
		Ni	0.76(5)	0.015(1)	
		Co	1.92(5)	0.038(1)	
		Si	42.8(6)	0.86(1)	
0.02	β	Fe	39.0(3)	1.17(1)	β-$Fe_{1.17(1)}Ni_{0.006(4)}Co_{0.034(3)}Si_{1.79(1)}$
		Ni	0.2(1)	0.006(4)	
		Co	1.12(9)	0.034(3)	
		Si	59.7(3)	1.79(1)	
	ε	Fe	53.4(7)	1.07(1)	ε-$Fe_{1.07(1)}Ni_{0.024(3)}Co_{0.034(3)}Si_{0.87(2)}$
		Ni	1.2(2)	0.024(3)	
		Co	1.7(1)	0.034(3)	
		Si	43.6(9)	0.87(2)	
0.03	β	Fe	39.4(9)	1.18(3)	β-$Fe_{1.18(3)}Ni_{0.01(1)}Co_{0.038(2)}Si_{1.77(2)}$
		Ni	0.4(4)	0.01(1)	
		Co	1.27(7)	0.38(2)	
		Si	59.1(8)	1.77(2)	
	ε	Fe	50.6(8)	1.01(2)	ε-$Fe_{1.01(2)}Ni_{0.078(8)}Co_{0.043(1)}Si_{0.87(1)}$
		Ni	3.9(4)	0.078(8)	
		Co	2.1(1)	0.043(1)	
		Si	43.4(3)	0.87(1)	

In addition, at high temperatures between 700–800 K, the ρ of the $0.005 \leq x \leq 0.03$ samples were about one order smaller in magnitude than that of the $x = 0$ sample. The remarkable reduction in the ρ of the Ni-substituted samples at high temperatures is probably due to the increase in μ_H, as shown in Fig. 6(b). In addition, Fig. 7 shows that with x increasing from 0.005 to 0.03, the ρ moderately decreases because the n_H slightly increases from $1.3(3) \times 10^{19}$ cm^{-3} to $2.2(3) \times 10^{19}$ cm^{-3}, as seen in Table 1.

The Seebeck coefficients (S) measured over temperatures in the 80–800K ranges are shown in Fig. 8. For pristine β-$FeSi_2$, the sign of S was positive at 80–195 K, indicating p-type semiconductor characteristic, and it turned negative in the 200–800 K window, indicating n-type semiconductor behavior. This variation is similar to that observed by Tani and Kido. They found that the Hall coefficient (R_H) was positive at temperatures lower than 160 K but turned negative at temperatures higher than 160 K.[33] This trend suggests that the conduction of non-doped β-$FeSi_2$ is affected by both electrons and holes, while their ratio is dependent on the temperature. In addition, due to the intrinsic properties of low n_H ($\sim 10^{16}$ cm^{-3}) and small bad gap (~ 0.7 eV), the absolute $|S|$ of pristine β-$FeSi_2$ remarkably decreased to 0 μV K^{-1} at high temperatures due to the bipolar effect. On the other hand, the S of all samples in the β-$Fe_{0.97-x}Ni_xCo_{0.03}Si_2$ system had a negative sign over the

measured temperature of 80–800 K, indicating that they behaved as n-type materials, in which the majority of charge carriers are electrons provided by the donors Co and Ni. In addition, at high temperatures, the absolute $|S|$ of β-$Fe_{0.97-x}Ni_xCo_{0.03}Si_2$ was significantly higher and more uniform compared with that of pure β-$FeSi_2$ because of the receded bipolar effect, due to which the n_H remarkably increased from 10^{16} to 10^{19}–10^{20} cm^{-3}. On the other hand, the $|S|$ decreased with x because of the increased ε-phase, as confirmed by the SEM micrographs and Rietveld analysis in the above sections. Furthermore, Fig. S3 (ESI†) shows the tendency of $|S|$ versus n_H of the $0.005 \leq x \leq 0.03$ samples at 300 K. The solid lines represent the values of $|S|$ by calculated using Mott's theory with several effective masses (m^*). The relationship of m^* and $|S|$ is defined by:

$$|S| = \frac{k_B^2 T}{3|e|\hbar^2}m^*\left(\frac{\pi}{3n_H}\right)^{2/3} \quad (3)$$

where $|S|$ is the absolute Seebeck coefficient, k_B is the Boltzmann constant, T is the temperature, m^* is the effective mass, $\hbar$ is the Planck constant, e is the elementary charge, and n_H is the carrier concentration.[48] An inverse proportionality between $|S|$ and n_H is implied in eqn (3), and Fig. S3 (ESI†) shows that a good fitting was obtained for $m^* = 0.9\ m_e$. Therefore, for the $0.005 \leq x \leq 0.03$ samples, the decline in $|S|$ is caused by not only the increase
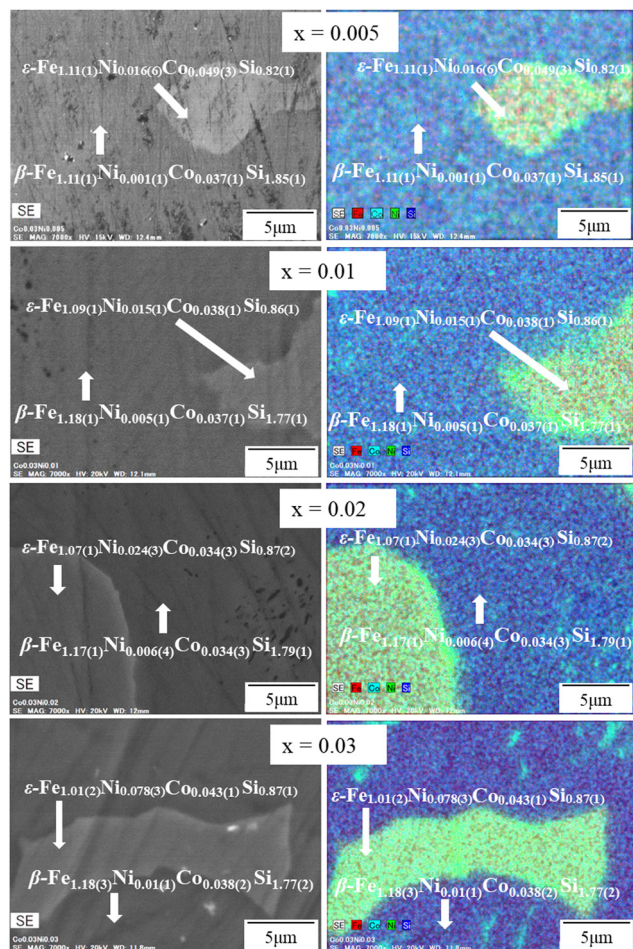
Fig. 5 The SEM-EDS color mapping of β-Fe$_{0.97-x}$Ni$_x$Co$_{0.03}$Si$_2$. Fe is mapped in red, Ni in green, Co in cyan, and Si in blue.

in ε-phase but also the slight increase in n_H from $1.3(3) \times 10^{19}$–$2.2(3) \times 10^{19}$cm^{-3}.

The temperature dependence of the power factor (PF = S^2/ρ) is shown in Fig. S4 (ESI†). The maximum PF of pure β-FeSi$_2$ was
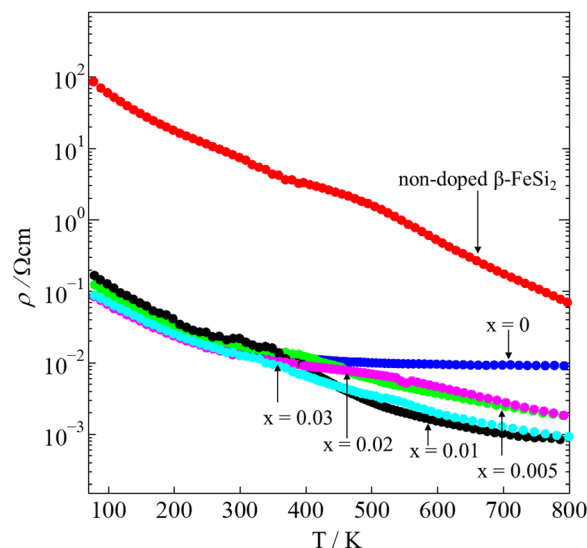

Fig. 7 The temperature dependence of the electrical resistivity (ρ) of non-doped β-FeSi$_2$ and β-Fe$_{0.97-x}$Ni$_x$Co$_{0.03}$Si$_2$.

only around 3.4 μW m^{-1} K^{-2} at 450 K, and then it significantly improved up to 900 μW m^{-1} K^{-2} at 800 K in the x = 0 sample (3% Co doping). More importantly, with Ni addition x = 0.01, the PF was further enhanced up to 2400 μW m^{-1} K^{-2} at 720 K. This improved PF is mainly influenced by the decrease in ρ. However, when we increased x up to 0.02 and 0.03, the PF decreased due to the reduction in $|S|$, as shown in Fig. 8. Hence, x = 0.01 is the optimum Ni substitution amount for enhancing the PF value.

The total thermal conductivity (κ) values of the samples at room temperature are summarized in Table 1, and the values moderately decrease with x. The temperature dependence of the κ of all samples is plotted in Fig. 9, which shows that the minimum values of κ were obtained for the $0.01 \leq x \leq 0.03$ samples. In addition, the Wiedemann–Franz law was used to calculate the electronic thermal conductivity ($\kappa_e = L_0\rho^{-1}T$, where κ_e is the electronic thermal conductivity, L_0 is the Lorenz
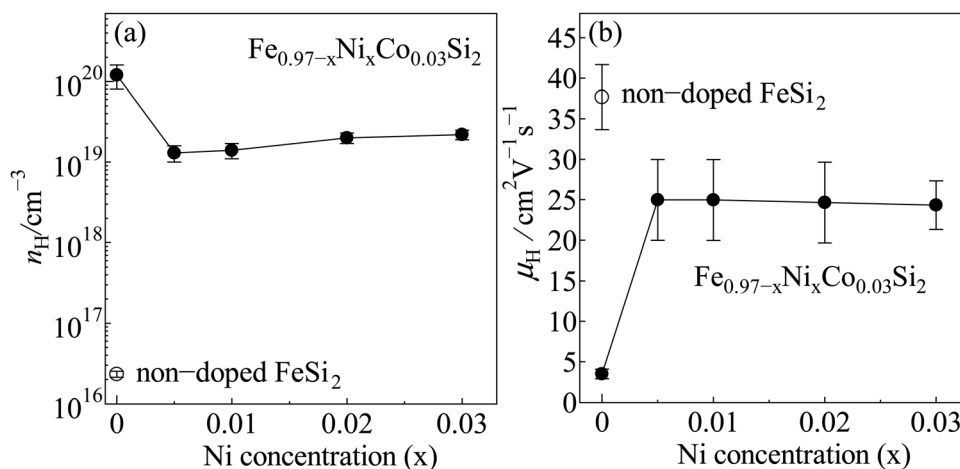

Fig. 6 (a) Carrier density (n_H) and (b) mobility (μ_H) of non-doped β-FeSi$_2$ and β-Fe$_{0.97-x}$Ni$_x$Co$_{0.03}$Si$_2$ at room temperature.
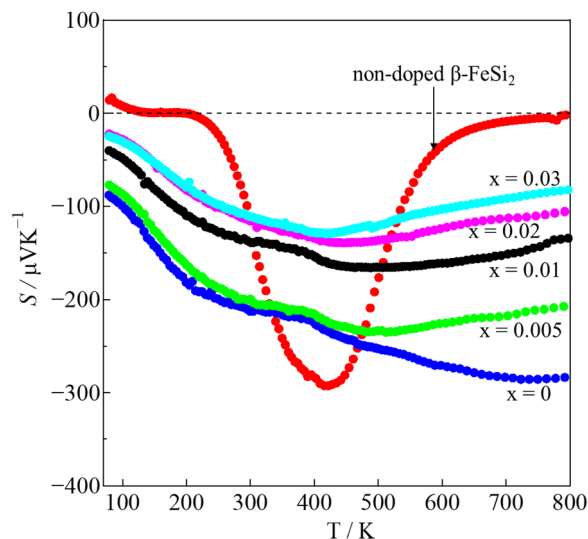
Fig. 8 The variation of the Seebeck coefficient (S) of non-doped β-FeSi$_2$ and β-Fe$_{0.97-x}$Ni$_x$Co$_{0.03}$Si$_2$.
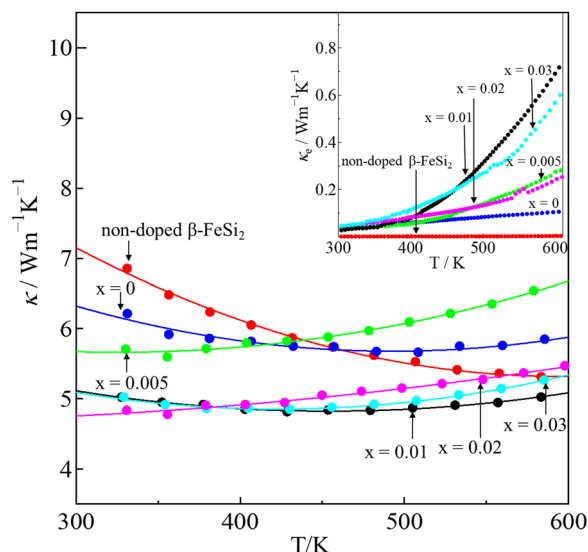
Fig. 9 The temperature dependence of the total thermal conductivity (κ) of non-doped β-FeSi$_2$ and β-Fe$_{0.97-x}$Ni$_x$Co$_{0.03}$Si$_2$; the electronic thermal conductivity (κ_e) is plotted in the inset.

number, ρ is the electrical resistivity, and T is the temperature). The scattering factor r of $-1/2$ (acoustic phonon scattering) and the experimental values of the Seebeck coefficients were used for calculating the L_0. The correlation between r and L_0 was defined as:

$$L_0 = \left(\frac{k_B}{e}\right)^2 \left[\frac{\left(r+\frac{7}{2}\right)F_{r+\frac{5}{2}}(\eta)}{\left(r+\frac{3}{2}\right)F_{r+\frac{1}{2}}(\eta)} - \left\{ \frac{\left(r+\frac{5}{2}\right)F_{r+\frac{3}{2}}(\eta)}{\left(r+\frac{3}{2}\right)F_{r+\frac{1}{2}}(\eta)} \right\}^2 \right], \quad (4)$$

where the function is given by: $F_n(\eta) = \int_0^\infty \frac{\chi^n}{1 + e^{\chi-\eta}}d\chi$, $\chi = \frac{E}{k_B T}$, $\eta = \frac{E_F}{k_B T}$. E_F represents the Fermi energy.[49] Then, L_0 was calculated by using eqn (4). As seen in Table 1, with x increasing from 0.005 to 0.03, the L_0 slightly increased. This trend indicates that the phase transition from semiconductor (β-FeSi$_2$) to metal (ε-FeSi) occurs because of Ni substitution. Consequently, the inset of Fig. 9 shows that the κ_e also increases with x. The increased κ_e should cause a negative impact on the total thermal conductivity ($\kappa = \kappa_e + \kappa_l$). It can be considered that the slight reduction in total thermal conductivity with Ni substitution, as shown in Fig. 9, is mainly caused by the reduction in lattice thermal conductivity (κ_l). This is possibly because of the electron–phonon interaction when dopants are introduced to the host material. A previous study shows a similar tendency of reduced κ when Co is introduced to β-FeSi$_2$.[34] In addition, the increasing number of pores or enlargement of pore size, as shown by the SEM images, can also be the reason behind the reduction in κ. The slight reduction in thermal conductivity observed in this study is mainly influenced by pore defects.

Fig. 10 shows the dimensionless figures of merit (ZT) calculated by using eqn (1). The ZT value is used to define the performance of any TE materials. As shown in the inset of Fig. 10, the maximum ZT of binary β-FeSi$_2$ was only 2.6×10^{-4} at 450 K. On the other hand, the ZT values of all β-Fe$_{0.97-x}$Ni$_x$Co$_{0.03}$Si$_2$ samples were much higher than that of non-doped β-FeSi$_2$. For the $x = 0$ sample, the highest ZT value was around 0.099 at 800 K. However, upon increasing to $x = 0.01$, the highest ZT enhanced up to 0.31 at 720 K due to the decrease in electrical resistivity and thermal conductivity. Then, the ZT decreased when $x = 0.02$ and 0.03 due to the reduction in the Seebeck coefficients; therefore, $x = 0.01$ is the
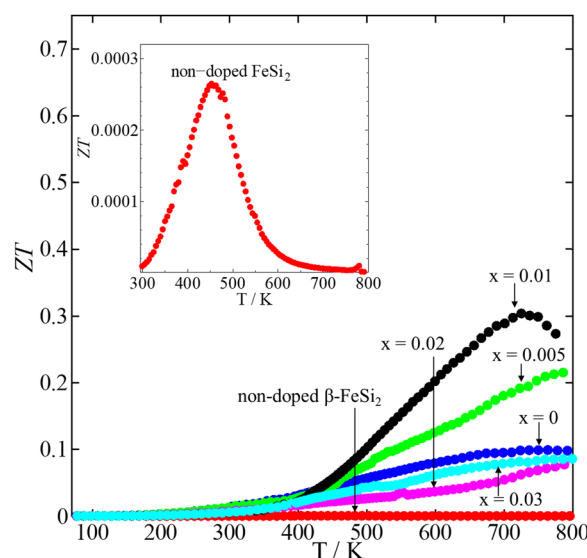

Fig. 10 The temperature dependence of the dimensionless figure of merit (ZT) of non-doped β-FeSi$_2$ and β-Fe$_{0.97-x}$Ni$_x$Co$_{0.03}$Si$_2$. The curve of non-doped β-FeSi$_2$ is magnified in the inset.

optimum Ni content in β-Fe$_{0.97-x}$Ni$_x$Co$_{0.03}$Si$_2$. The maximum ZT obtained in this work is lower than that of β-FeSi$_2$ with 16% Ir doping ($ZT = 0.6$) because Ir-doped β-FeSi$_2$ had lower electrical resistivity owing to the high carrier density.[32] However, the highest ZT value observed in this study ($ZT_{max} = 0.31$) is remarkably higher than those of the previously reported β-Fe$_{0.93}$Co$_{0.07}$Si$_2$ sample ($ZT_{max} = 0.18$) fabricated by the magnesiothermic process,[23] β-Fe$_{0.97}$Co$_{0.03}$Si$_2$ sample ($ZT_{max} = 0.15$) prepared by the pulse plasma sintering (PPS) method,[38] β-Fe$_{0.98}$Co$_{0.02}$Si$_2$ ($ZT_{max} = 0.15$) prepared by spark plasma sintering (SPS),[42] β-Fe$_{0.95}$Co$_{0.05}$Si$_2$ sample ($ZT_{max} = 0.14$) prepared by the SPS method,[44] β-Fe$_{0.95}$Co$_{0.05}$Si$_{1.958}$ Ge$_{0.042}$ ($ZT_{max} = 0.11$) prepared by the pressure sintering method,[50] and β-FeSi$_2$ with some dopants (Zr, Nb, and Ti).[51]

4. Conclusions

In summary, non-doped β-FeSi$_2$ and β-Fe$_{0.97-x}$Ni$_x$Co$_{0.03}$Si$_2$ ($x = 0.005, 0.01, 0.02,$ and 0.03) were fabricated by the arc-melting method. It was observed that heat treatment is necessary to transform the metallic phase into the semiconducting phase. With increasing x, the results show that more metallic ε-phases were formed, and the distribution of Co in the materials became less homogeneous, resulting in a decrease in carrier density. However, the mobility significantly improved from 3.5(6) to 25(5) cm^2 V^{-1} s^{-1} with Ni substitution; therefore, the electrical resistivity effectively decreased by one order of magnitude at high temperatures. The Seebeck coefficient decreased with x due to the formation of the ε-phase. The slight reduction in thermal conductivity observed after Ni addition is probably owing to the enlargement of the pores. As a result, the highest ZT of 0.31 was achieved in the $x = 0.01$ sample at 720 K because of the reduced electrical resistivity and a slight reduction in thermal conductivity. The maximum ZT obtained in this study is remarkably higher than those reported previously for Co-doped β-FeSi$_2$,[23,34,38,42,44] β-FeSi$_2$ co-doped with Co and Ge,[50] and β-FeSi$_2$ doped with other elements (Zr, Nb, and Ti).[51] Therefore, the abundant and eco-friendly β-Fe$_{0.97-x}$Ni$_x$Co$_{0.03}$Si$_2$ compound can be a promising thermoelectric material for harvesting industrial waste heat.

Author contributions

The concept of the study is proposed by H. Nakatsugawa, S. Sam, and Y. Okamoto. The investigation was done by S. Sam and H. Nakatsugawa. The data interpretation and analysis are conducted by S. Sam, H. Nakatsugawa, and Y. Okamoto. The original draft was prepared and written by S. Sam and H. Nakatsugawa. All authors have reviewed and approved the submission of the manuscript.

Conflicts of interest

The authors declare that there is no competing financial interest.

References

1 R. Fitriani, B. D. Ovik, M. C. Long, M. Barma, M. F. M. Riaz, S. M. Sabri and R. Said, *Renewable Sustainable Energy Rev.*, 2016, **64**, 635–659.

2 M. Hamid Elsheikh, D. A. Shnawah, M. F. M. Sabri, S. B. M. Said, M. Haji Hassan, M. B. Ali Bashir and M. Mohamad, *Renewable Sustainable Energy Rev.*, 2014, **30**, 337–355.

3 R. Sok and J. Kusaka, *Appl. Therm. Eng.*, 2023, **219**, 119530.

4 R. Sok and J. Kusaka, *Int. J. Heat Mass Transfer*, 2023, **202**, 123718.

5 J. Yang and F. R. Stabler, *J. Electron. Mater.*, 2009, **38**, 1245–1251.

6 H. J. Goldsmid, in *Introduction to Thermoelectricity*, ed. H. Robert, J. Chennupati, K. Yoshiyuki, M. O. Richard, P. Jürgen, S. Tae-Yeon, U. Shin-ichi and M. W. Zhiming, Springer Berlin Heidelberg, Berlin, Heidelberg, 2nd edn, 2016, pp. 9–24.

7 H. Fukutomi, Y. Konno, K. Okayasu, M. Hasegawa and H. Nakatsugawa, *Mater. Sci. Eng., A*, 2009, **527**, 61–64.

8 H. Nakatsugawa, M. Kubota and M. Saito, *J. Jpn. Inst. Met.*, 2015, **79**, 597–606.

9 H. Nakatsugawa, M. Saito and Y. Okamoto, *J. Electron. Mater.*, 2017, **46**, 3262–3272.

10 H. Nakatsugawa, M. Saito and Y. Okamoto, *Mater. Trans.*, 2019, **60**, 1051–1060.

11 X. Chen, H. Zhang, Y. Zhao, W.-D. Liu, W. Dai, T. Wu, X. Lu, C. Wu, W. Luo, Y. Fan, L. Wang, W. Jiang, Z.-G. Chen and J. Yang, *ACS Appl. Mater. Interfaces*, 2019, **11**, 22457–22463.

12 X.-Q. Chen, S.-J. Fan, C. Han, T. Wu, L.-J. Wang, W. Jiang, W. Dai and J.-P. Yang, *Rare Met.*, 2021, **40**, 2017–2025.

13 S. Katsuyama, H. Matsushima and M. Ito, *J. Alloys Compd.*, 2004, **385**, 232–237.

14 H. Nakatsugawa, T. Ozaki, H. Kishimura and Y. Okamoto, *J. Electron. Mater.*, 2020, **49**, 2802–2812.

15 T. Sakata, Y. Sakai, H. Yoshino, H. Fujii and I. Nishida, *J. Less-Common Met.*, 1978, **61**, 301–308.

16 L. Pauling and A. M. Soldate, *Acta Crystallogr.*, 1948, **1**, 212–216.

17 Y. Dusausoy, J. Protas, R. Wandji and B. Roques, *Acta Crystallogr., Sect. B: Struct. Crystallogr. Cryst. Chem.*, 1971, **27**, 1209–1218.

18 O. Caballero-Calero, J. R. Ares and M. Martín-González, *Adv. Sustainable Syst.*, 2021, **5**, 2100095.

19 U. Stöhrer, R. Voggesberger, G. Wagner and U. Birkholz, *Energy Convers. Manage.*, 1990, **30**, 143–147.

20 Y. Isoda and H. Udono, in *Thermoelectrics and its Energy Harvesting*, ed. D. M. Rowe, CRC Press, 1st edn, 2012, pp. 18-1–18-25.

21 R. Girlanda, E. Piparo and A. Balzarotti, *J. Appl. Phys.*, 1994, **76**, 2837–2840.

22 S. J. Clark, H. M. Al-Allak, S. Brand and R. A. Abram, *Phys. Rev. B: Condens. Matter Mater. Phys.*, 1998, **58**, 10389–10393.

23 S. Le Tonquesse, Z. Verastegui, H. Huynh, V. Dorcet, Q. Guo, V. Demange, C. Prestipino, D. Berthebaud, T. Mori and M. Pasturel, *ACS Appl. Energy Mater.*, 2019, **2**, 8525–8534.

24 N. Liu, S. E. Rezaei, W. A. Jensen, S. Song, Z. Ren, K. Esfarjani, M. Zebarjadi and J. A. Floro, *Adv. Funct. Mater.*, 2019, **29**, 1903157.

25 X. Du, P. Hu, T. Mao, Q. Song, P. Qiu, X. Shi and L. Chen, *ACS Appl. Mater. Interfaces*, 2019, **11**, 32151–32158.

26 H. Y. Chen, X. B. Zhao, C. Stiewe, D. Platzek and E. Mueller, *J. Alloys Compd.*, 2007, **433**, 338–344.

27 A. Binti Abdullah Zaik, F. Liana Binti Mohd. Redzuan, S. Ahmad Zaki Bin Shaikh Salim, A. Faiz Bin Mohammad, M. Fitri Bin Mohd. Yakub and M. Takeda, *Mater. Today: Proc.*, 2022, **65**, 2979–2985.

28 W. Liu, X. Yan, G. Chen and Z. Ren, *Nano Energy*, 2012, **1**, 42–56.

29 J. J. Gong, A. J. Hong, J. Shuai, L. Li, Z. B. Yan, Z. F. Ren and J.-M. Liu, *Phys. Chem. Chem. Phys.*, 2016, **18**, 16566–16574.

30 Z. Chen, X. Zhang, J. Ren, Z. Zeng, Y. Chen, J. He, L. Chen and Y. Pei, *Nat. Commun.*, 2021, **12**, 3837.

31 X. B. Zhao, H. Y. Chen, E. Müller and C. Drasar, *Appl. Phys. A: Mater. Sci. Process.*, 2005, **80**, 1123–1127.

32 P. Qiu, J. Cheng, J. Chai, X. Du, X. Xia, C. Ming, C. Zhu, J. Yang, Y. Sun, F. Xu, X. Shi and L. Chen, *Adv. Energy Mater.*, 2022, **12**, 2200247.

33 J. Tani and H. Kido, *J. Appl. Phys.*, 1998, **84**, 1408–1411.

34 J. Tani and H. Kido, *Jpn. J. Appl. Phys.*, 2001, **40**, 3236.

35 J. Tani and H. Kido, *J. Appl. Phys.*, 2000, **88**, 5810–5813.

36 M. Ito, H. Nagai, E. Oda, S. Katsuyama and K. Majima, *J. Appl. Phys.*, 2002, **91**, 2138–2142.

37 F. L. B. M. Redzuan, I. Mikio and T. Masatoshi, *J. Mater. Sci.*, 2018, **53**, 7683–7690.

38 F. Dąbrowski, Ł. Ciupiński, J. Zdunek, J. Kruszewski, R. Zybała, A. Michalski and K. Jan Kurzydłowski, *Mater. Today: Proc.*, 2019, **8**, 531–539.

39 S. Sam, H. Nakatsugawa and Y. Okamoto, *Jpn. J. Appl. Phys.*, 2022, **61**, 111002.

40 S. Sam, S. Odagawa, H. Nakatsugawa and Y. Okamoto, *Materials*, 2023, **16**, 927.

41 M. Ohtaki, D. Ogura, K. Eguchi and H. Arai, *Chem. Lett.*, 1993, 1067–1070.

42 X. Qu, S. Lü, J. Hu and Q. Meng, *J. Alloys Compd.*, 2011, **509**, 10217–10221.

43 K. Nogi and T. Kita, *J. Mater. Sci.*, 2000, **35**, 5845–5849.

44 L. Abbassi, D. Mesguich, D. Berthebaud, S. Le Tonquesse, B. Srinivasan, T. Mori, L. Coulomb, G. Chevallier, C. Estournès, E. Flahaut, R. Viennois and M. Beaudhuin, *Nanomaterials*, 2021, **11**, 2852.

45 F. Dąbrowski, Ł. Ciupiński, J. Zdunek, W. Chromiński, M. Kruszewski, R. Zybała, A. Michalski and K. J. Kurzydłowski, *Arch. Metall. Mater.*, 2021, **66**, 1157–1162.

46 S. Brehme, G. Behr and A. Heinrich, *J. Appl. Phys.*, 2001, **89**, 3798–3803.

47 T. Takeuchi, in *Thermoelectrics and its Energy Harvesting*, ed. D. M. Rowe, Taylor & Francis Group, Abingdon, UK, 1st edn, 2017, pp. 7-1–7-27.

48 N. F. Mott, *J. Non-Cryst. Solids*, 1968, **1**, 1–17.

49 L.-D. Zhao, S.-H. Lo, J. He, H. Li, K. Biswas, J. Androulakis, C.-I. Wu, T. P. Hogan, D.-Y. Chung, V. P. Dravid and M. G. Kanatzidis, *J. Am. Chem. Soc.*, 2011, **133**, 20476–20487.

50 S. W. Kim, M. K. Cho, Y. Mishima and D. C. Choi, *Intermetallics*, 2003, **11**, 399–405.

51 M. Ito, H. Nagai, S. Katsuyama and K. Majima, *J. Alloys Compd.*, 2001, **315**, 251–258.